



Global Biogeochemical Cycles

RESEARCH ARTICLE

10.1002/2014GB004832

Key Points:

- First data-driven global regionalized CO₂ budget for continental shelf seas
- Arctic shelves contribute disproportionately to global coastal CO₂ sink
- Seasonality of coastal FCO₂ can partly be explained by temperature and NPP

Supporting Information:

- Readme
- Table S1

Correspondence to:

G. G. Laruelle,
goulven.gildas.laruelle@ulb.ac.be

Citation:

Laruelle, G. G., R. Lauerwald, B. Pfeil, and P. Regnier (2014), Regionalized global budget of the CO₂ exchange at the air-water interface in continental shelf seas, *Global Biogeochem. Cycles*, 28, 1199–1214, doi:10.1002/2014GB004832.

Received 14 FEB 2014

Accepted 4 OCT 2014

Accepted article online 7 OCT 2014

Published online 11 NOV 2014

Regionalized global budget of the CO₂ exchange at the air-water interface in continental shelf seas

Goulven G. Laruelle^{1,2}, Ronny Lauerwald^{1,3}, Benjamin Pfeil⁴, and Pierre Regnier¹

¹Department of Earth and Environmental Sciences, Université Libre de Bruxelles, Brussels, Belgium, ²Department of Earth Sciences-Geochemistry, Faculty of Geosciences, Utrecht University, Utrecht, Netherlands, ³Institut Pierre-Simon Laplace, CNRS-FR636, Guyancourt, France, ⁴Bjerknes Centre for Climate Research, University of Bergen, Bergen, Norway

Abstract Over the past decade, estimates of the atmospheric CO₂ uptake by continental shelf seas were constrained within the 0.18–0.45 Pg C yr⁻¹ range. However, most of those estimates are based on extrapolations from limited data sets of local flux measurements ($n < 100$). Here we propose to derive the CO₂ air-sea exchange of the shelf seas by extracting $3 \cdot 10^6$ direct surface ocean CO₂ measurements from the global database SOCAT (Surface Ocean CO₂ Atlas), atmospheric CO₂ values from GlobalVIEW and calculating gas transfer rates using readily available global temperature, salinity, and wind speed fields. We then aggregate our results using a global segmentation of the shelf in 45 units and 152 subunits to establish a consistent regionalized CO₂ exchange budget at the global scale. Within each unit, the data density determines the spatial and temporal resolutions at which the air-sea CO₂ fluxes are calculated and range from a 0.5° resolution in the best surveyed regions to a whole unit resolution in areas where data coverage is limited. Our approach also accounts, for the first time, for the partial sea ice cover of polar shelves. Our new regionalized global CO₂ sink estimate of 0.19 ± 0.05 Pg C yr⁻¹ falls in the low end of previous estimates. Reported to an ice-free surface area of $22 \cdot 10^6$ km², this value yields a flux density of 0.7 mol C m⁻² yr⁻¹, ~40% more intense than that of the open ocean. Our results also highlight the significant contribution of Arctic shelves to this global CO₂ uptake (0.07 Pg C yr⁻¹).

1. Introduction

The carbon cycle in continental shelf seas has been profoundly disturbed by human activities since the beginning of the industrial revolution [Bauer *et al.*, 2013; Regnier *et al.*, 2013]. Changes in carbon cycling results from the increasing amounts of organic and inorganic carbon from rivers [Meybeck, 1982] and tidal wetlands [Cai, 2011; Bauer *et al.*, 2013] as well as from the modified intensity of the carbon dioxide (CO₂) exchange at the air-water interface in coastal waters [Mackenzie *et al.*, 2012]. Globally, the exact magnitude of this change is still highly unclear [Cai, 2011; Bauer *et al.*, 2013; Regnier *et al.*, 2013], and the present-day exchange of CO₂ between the atmosphere and continental shelf seas remains loosely constrained, with an uncertainty as large as 50–100% [Bauer *et al.*, 2013]. Before the respective contributions of the natural and anthropogenic components of this exchange can be dissociated, it is important to better quantify the bulk flux and, in particular, the extent to which the current CO₂ uptake rate of the coastal ocean could differ from that of the surrounding open ocean.

The limited number of available local studies reports areas of very intense CO₂ exchanges at the air-water interface, which act both as sources [Friederich *et al.*, 2002; Cai *et al.*, 2003; Shadwick *et al.*, 2011] or sinks [Degrandpré *et al.*, 2002; Thomas *et al.*, 2004; Borges *et al.*, 2006] with respect to the atmosphere. These local estimates have been used to establish global budgets of the air-sea CO₂ flux [Borges, 2005; Cai *et al.*, 2006; Laruelle *et al.*, 2010; Cai, 2011; Chen *et al.*, 2013; Dai *et al.*, 2013], and the first global extrapolation, derived from only one local estimate, suggested an atmospheric sink of CO₂ as large as 1.0 Pg C yr⁻¹ [Tsunogai *et al.*, 1999]. With the growing number of measurements over the years (27 in Borges [2005]; 37 in Cai *et al.* [2006]; and 62 in Laruelle *et al.* [2010]) the estimates were revised downward, and the most recent budgets fall within the 0.21–0.4 Pg C yr⁻¹ range [Chen and Borges, 2009; Laruelle *et al.*, 2010; Cai, 2011; Chen *et al.*, 2013; Dai *et al.*, 2013]. The discrepancies between these estimates can partly be explained by the skewed distribution of local studies and by different definitions of the continental shelf domain [Laruelle *et al.*, 2010]. This range of values yields average flux densities comprised between -0.7 and -1.2 mol C m⁻² yr⁻¹, somewhat higher than that of the open ocean (around -0.5 mol C m⁻² yr⁻¹), which suggests that, per unit surface area, continental shelf seas could be a more efficient CO₂ sink.

The current development of the community-driven global ocean FCO_2 data product SOCAT (for Surface Ocean CO_2 Atlas, Pfeil *et al.*, 2013; Bakker *et al.*, 2014) now permits to improve these estimates [Chen *et al.*, 2013] and to perform increasingly refined regionalized budgets [Laruelle *et al.*, 2013; Regnier *et al.*, 2013]. Here we present a seasonally and spatially resolved data-driven budget for the CO_2 air-sea exchange using the global data product of marine CO_2 partial pressure measurements (pCO_2) SOCAT v2.0, together with global wind speed and atmospheric forcings as well as atmospheric CO_2 data compiled in GlobalVIEW. Although the data coverage remains heterogeneous within SOCAT, it contains over $3 \cdot 10^6$ coastal points and allows constraining spatially and temporally resolved regional carbon budgets for several regions of the world. For instance, our calculations for best surveyed continental shelves seas provide monthly estimates of the CO_2 exchange at a 0.5° resolution.

2. Methods

2.1. Strategy

The $3 \cdot 10^6$ water pCO_2 values derived from in situ measurements (SOCAT 2.0 database; Bakker *et al.* [2014]) were used in conjunction with global environmental databases to calculate instantaneous CO_2 exchange rates through the air-water interface at given locations ($\overline{FCO_2}$). Then, these $\overline{FCO_2}$ were integrated using four different spatial integration methods adapted to the data density of the region considered to provide regionalized yearly CO_2 flux (FCO_2). To comply with the most widely used conventions in the literature, in sections 3 and 4, $\overline{FCO_2}$ and FCO_2 are expressed in $\text{mol C m}^{-2} \text{yr}^{-1}$ and Tg C yr^{-1} , respectively. Positive values correspond to an outgassing of CO_2 toward the atmosphere, while negative values correspond to a sink of CO_2 for the atmosphere. In section 2, the units correspond to those of the raw data used for the calculation (i.e., μatm for pCO_2 , $^\circ\text{Celsius}$ for sea surface temperature, and m s^{-1} for wind speed). Conversion factors were then applied to express the final $\overline{FCO_2}$ and FCO_2 within the aforementioned units and dimensions.

2.2. Exchange Rate Calculation

For each SOCAT data point, an instantaneous $\overline{FCO_2}$ was calculated using Liss and Slater's [1974] formulation and Takahashi *et al.*'s [2009] parameterization:

$$\overline{FCO_2} = k \cdot K'_0 \cdot \Delta pCO_2 \quad (1)$$

where k corresponds to the gas transfer velocity (cm h^{-1}), K'_0 corresponds to the Henry's constant of CO_2 in sea water, and ΔpCO_2 is the difference in CO_2 partial pressure between water and the atmosphere. The parameter k is defined as follows:

$$k = \Gamma C U^2 \left(\frac{Sc}{660} \right)^{-1/2} \quad (2)$$

with Γ as the transfer coefficient set at 0.26 following Takahashi *et al.* [2009], U is the wind speed 10 m above the sea surface, extracted from the 0.25° resolution cross-calibrated, multiplatform (CCMP) wind speed database [Atlas *et al.*, 2011], C is a correction factor to account for the use of a climatology for wind speed defined by Jiang *et al.* [2008] and Sc is the Schmidt number.

$$C = \frac{\frac{1}{n} \sum_j U_j^2}{U_{\text{mean}}^2} \quad (3)$$

where U_j is the high-frequency wind speed, U_{mean} is the monthly mean wind speed over the study period, and n is the number of available wind speeds in each month. The Schmidt number (Sc) is computed as in Wanninkhof [1992]:

$$Sc = 2073.1 - 125.62 \text{ SST} + 3.6276 \text{ SST}^2 - 0.043219 \text{ SST}^3 \quad (4)$$

where SST is the sea surface temperature taken from SOCAT or extracted from the 1° resolution World Ocean Atlas [Locarnini *et al.*, 2010] where data are unavailable in SOCAT.

K'_0 was calculated from Weiss [1974]:

$$\ln K'_0 = -58.0931 + 90.5069 \left(\frac{100}{T_{\text{abs}}} \right) + 22.2940 \ln \left(\frac{100}{T_{\text{abs}}} \right) + S \left[\begin{array}{l} 0.027766 + 0.025888 \left(\frac{100}{T_{\text{abs}}} \right) \\ + 0.0050578 \left(\frac{100}{T_{\text{abs}}} \right)^2 \end{array} \right] \quad (5)$$

where T_{abs} and S are the absolute temperature of surface water in Kelvin and the salinity, respectively. S is also taken from SOCAT when available or extracted from the World Ocean Atlas [Antonov *et al.*, 2010] otherwise.

The following equation provides the $p\text{CO}_2$ in the air:

$$(p\text{CO}_2)_{\text{air}} = X\text{CO}_2(P_{\text{baro}} - P_{\text{sw}}) \quad (6)$$

where P_{baro} is the barometric pressure at sea surface and P_{sw} is the water vapour at the temperature and salinity of the mixed layer water. $X\text{CO}_2$ is the weekly mean CO_2 concentration for dry air extracted from the GLOBALVIEW-CO2 [2012] database. P_{sw} was calculated assuming 100% humidity using sea surface temperature and salinity from the World Ocean Atlas [Antonov *et al.*, 2010; Locarnini *et al.*, 2010] and P_{baro} is the monthly mean barometric pressure at the sea surface from the NCEP/NCAR Reanalysis database [Kalnay *et al.*, 1996]. The sea water $p\text{CO}_2$ used to calculate the air-water $p\text{CO}_2$ gradient was derived from the recommended fugacity ($f\text{CO}_2$) provided by the SOCAT v2.0 data product [Bakker *et al.*, 2014], using the equation reported in Takahashi *et al.* [2012]:

$$(p\text{CO}_2)_{\text{sw}} = f\text{CO}_2(1.00436 - 4.669 \cdot 10^{-5} \text{ SST}) \quad (7)$$

2.3. Segmentation Description

The segmentation used to define continental shelf regions and their geographic extent is described extensively in Laruelle *et al.* [2013]. In this work, the outer limit of the shelf is characterized by the shelf break, as opposed to the 200 m isobaths used in many other studies [Walsh, 1988; Borges *et al.*, 2005; Takahashi *et al.*, 2009; Laruelle *et al.*, 2010; Wanninkhof *et al.*, 2013]. The depth of the shelf break was calculated, for each Coastal Segmentation and related CATchments (COSCAT), using a high-resolution global bathymetric database [Laruelle *et al.*, 2013]. This delineation excludes internal waters such as estuaries, fjords, lagoons, or tidal marshes. The world's continental shelf is divided into 152 coastal segments called COSCATs (for Coastal Segmentation and related CATchments) of roughly homogeneous physical, geological, and climatological properties [Meybeck *et al.*, 2006]. These regions are further aggregated into larger entities designed to account for larger-scale physical and oceanographic processes such as coastal currents and large-scale climatic zones following the classification suggested by Liu *et al.* [2010]. These 45 larger regions are named MARCATS (for MARgins and CATchment Segmentation) and regrouped, on average, three COSCATs per unit [Laruelle *et al.*, 2013].

In our regionalized calculation, the COSCAT is the unit at which all analyses were performed and were subsequently scaled up or aggregated to MARCATS resolution. High-resolution Geographic Information System (GIS) files describing the geographic limits of each COSCAT were used to determine the association of each SOCAT sampling location to a given COSCAT and depth interval. Within each COSCAT, up to 10 depth intervals were defined depending on the depth of the shelf break [Laruelle *et al.*, 2013]. The intervals are bounded by the following isobaths: 20 m, 50 m, 80, 120 m, 150 m, 200 m, 350 m, 500 m, 750 m, and 1000 m.

2.4. Integration Methods

Our analysis does not account for decadal or interannual variations, and the data used are limited to the 1990–2011 period. All years were treated equally, and the effect of El Niño or other similar perturbations were not excluded from the study. Using data collected over the last two decades allows for a very good spatial coverage but potentially ignores recent temporal trends in $f\text{CO}_2$. Four different spatial integration methods were used to calculate the $f\text{CO}_2$ in each COSCAT depending on the data coverage (Table 1).

Method 1. In the case of highest data density within a COSCAT segment, the method used to calculate the $f\text{CO}_2$ provides a 0.5° resolution in space and a monthly resolution in time. A regular, half-degree resolution grid centered on the intersection between the equator and Greenwich's meridian was used, and the water surface area within each grid cell was calculated by GIS, excluding the parts that covered the continental

Table 1. Number and Cumulated Surface Areas of COSCAT Used for Each Type of Spatial and Temporal Integration Method^a

	Monthly	Seasonally	Yearly
Grid	23 COSCATs 5.0 · 10 ⁶ km ² σ = 0.18 mol C m ⁻² yr ⁻¹ (three stars)	17 COSCATs 3.4 · 10 ⁶ km ² σ = 0.20 mol C m ⁻² yr ⁻¹ (three stars)	
Depth	7 COSCATs 1.2 · 10 ⁶ km ² σ = 0.31 mol C m ⁻² yr ⁻¹ (two stars)	5 COSCATs 1.3 · 10 ⁶ km ² σ = 0.42 mol C m ⁻² yr ⁻¹ (two stars)	26 COSCATs 5.8 · 10 ⁶ km ² σ = 0.44 mol C m ⁻² yr ⁻¹ (two stars)
COSCAT	2 COSCATs 0.7 · 10 ⁶ km ² σ = 0.49 mol C m ⁻² yr ⁻¹ (two stars)	7 COSCATs 0.7 · 10 ⁶ km ² σ = 0.63 mol C m ⁻² yr ⁻¹ (one star)	24 COSCATs 3.4 · 10 ⁶ km ² σ = 1.01 mol C m ⁻² yr ⁻¹ (one star)
MARCATS		6 COSCATs 0.9 · 10 ⁶ km ²	27 COSCATs 5.8 · 10 ⁶ km ²

^aThe standard deviation predicted by the uncertainty analysis is also provided. Three stars mean “good,” two stars, “fair,” and one star, “poor.”

masses and other contiguous COSCATs. This method can be seen as a finer analog to *Takahashi et al.'s* [2009] grid for the open ocean.

Within each cell, the calculated $\overline{FCO_2}$ were averaged for every month, first performing year-specific averages and then averaging these averages to minimize potential bias toward overrepresented years. The monthly mean CO₂ exchange rate $(\overline{FCO_2})_m$ with the atmosphere was then obtained using the following formula:

$$(\overline{FCO_2})_m = \frac{\sum_i \overline{FCO_2} \times S_i}{\sum_i S_i} \quad (8)$$

where S_i is the surface area of the grid cell i , and the numeration is performed over all cells within a given COSCAT. This monthly weighted average $(\overline{FCO_2})_m$ was then multiplied by the total surface area S of the COSCAT and the molar mass of carbon to obtain a value for $(FCO_2)_m$, in g C month⁻¹ yr⁻¹. The sum of all monthly FCO_2 provided an estimate of the annual FCO_2 .

Application of this method was limited to COSCATs with at least 20% surface area coverage of the COSCAT (for a given month) and at least data for 11 out of 12 months. When 1 month was missing, its monthly $(\overline{FCO_2})_m$ was assumed to be the average of the preceding and following months. A lower temporal coverage led to a looser temporal integration (per season or, in case of very poor coverage, per year). The seasons were defined using complete months starting with January, February, and March to represent boreal winter and July, August, and September to represent austral winter.

Method 2. In case of spatial coverage <10% of the COSCAT surface area, the integration method used remained conceptually similar to Method 1 but uses depth intervals instead of grid cells to perform the calculations. These depth intervals are larger entities than 0.5° resolution cells but are treated similarly. Their number varies from a COSCAT to the other between 4 and 10 depending on the depth of the shelf break.

Method 3. In case of very low spatial coverage (<1% of the COSCAT surface area), no spatial discretization was used and the integration was performed at the scale of the entire COSCAT segment, which was treated as a single large cell.

Method 4. Finally, integration at the MARCATS scale was performed for the COSCAT segments devoid of data in the SOCAT database but belonging to a MARCATS for which FCO_2 were available for the neighboring COSCATs. In such case, the average $\overline{FCO_2}$ derived from all COSCATs containing data within the MARCATS was extrapolated to the COSCATs with no data.

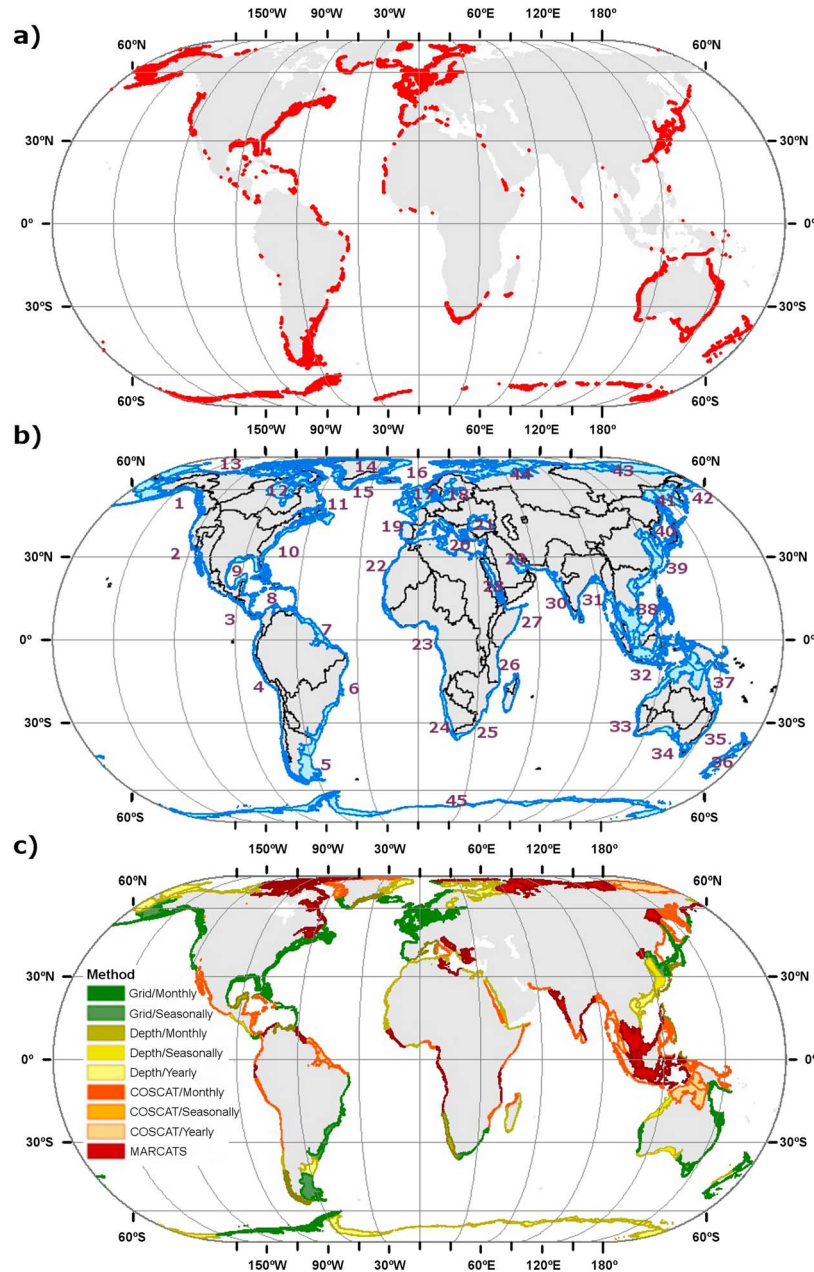


Figure 1. (a) Global distribution of SOCAT v2.0 sampling locations used for this study. (b) Geographic extent and limits of the COSCAT (blue) and MARCATS (black). The purple numbering corresponds to the MARCATS segment numbers. (c) Integration methods used for each COSCAT segment.

Finally, the effect of sea ice cover on the available exchange surface area at the air-water interface is taken into account in Polar Regions by calculating a monthly ice cover index. For each month, the fraction of the COSCAT covered in ice was considered impermeable to gas transfer and the monthly FCO_2 was linearly scaled down to the ice-free surface area of the considered COSCAT. The average monthly ice coverage for each COSCAT were calculated by GIS using 25 km resolution monthly ice concentrations over the 1990–2011 provided by the NSIDC (National Snow and Ice Cover Data) [Cavalieri *et al.*, 1996].

Figure 1c summarizes the method applied to each COSCAT globally, while Table 1 lists the number of COSCATs treated by each method and their cumulative surface area. Altogether, a FCO_2 could be calculated

for 74% of the surface of the continental shelf seas using Methods 1 to 3 and 22% was derived using those of contiguous COSCATs (Method 4). The only MARCATs totally devoid of data in the SOCAT database are the Hudson Bay, the Black Sea, and the Persian Gulf (MARCATs 12, 21, and 29, respectively), and together these three units account for the remaining surface area of the continental shelves (~4%).

2.5. Uncertainty Quantification

The uncertainties associated to each integration method were calculated by performing random subsampling within COSCAT 827, which is the best monitored COSCAT and thus used as reference. This COSCAT was treated as a complete entity with perfect spatial and temporal coverage. The data coverage of each subsample was thus calculated with respect to the reference COSCAT. Over 1000 simulations were performed for ranges of spatial and temporal coverage defining the application criteria for each of the integration methods described in section 2.4. The resulting standard deviations around the mean $\overline{FCO_2}$ values of the reference COSCAT were used as quantification of uncertainty associated to each integration method. As a test, the same calculations were performed using COSCATs 403 and 1410, which have a similarly good data coverage, confirming that the standard deviations are not significantly different. The average standard deviations in $\text{mol C m}^{-2} \text{yr}^{-1}$ retained as quantification of the confidence associated to each method are listed in Table 1. A more qualitative rating was also used and assigns “three stars” to COSCATs for which $\sigma < 0.25 \text{ mol C m}^{-2} \text{yr}^{-1}$, “two stars” if $\sigma < 0.5 \text{ mol C m}^{-2} \text{yr}^{-1}$, and “one star” if $\sigma > 0.5 \text{ mol C m}^{-2} \text{yr}^{-1}$. This star rating is provided for each COSCAT in Table S1 in the supporting information. “Three stars” is considered good, “two stars”, fair, and “one star”, poor.

The confidence interval for the global FCO_2 estimate was obtained by performing 10,000 Monté Carlo calculations in which the FCO_2 for each COSCAT was distributed according to normal distributions using the actual FCO_2 as average and the σ associated to the integration method as standard deviations. The distribution of the resulting 10,000 estimates of global FCO_2 were used to define a confidence interval between the 2.5th and 97.5th percentiles.

3. Results

3.1. Global Distribution of FCO_2

The yearly $\overline{FCO_2}$ calculated per COSCAT (Figure 2a) vary from $-5.5 \text{ mol C m}^{-2} \text{yr}^{-1}$ in Southern Greenland waters to $5.1 \text{ mol C m}^{-2} \text{yr}^{-1}$ along the coast of Morocco. Of 144 COSCATs, 91 behave as CO_2 sinks among which 14 display rates lower than $-3 \text{ mol C m}^{-2} \text{yr}^{-1}$, all of them located north of 60°N , along Eastern Siberia or Southern Greenland. Similarly, the five COSCATs characterized by $\overline{FCO_2}$ between -3 and $-2 \text{ mol C m}^{-2} \text{yr}^{-1}$ all belong to Arctic shelves, the Canadian archipelagos, or the Western North Pacific coast at latitudes $>60^\circ\text{N}$. The distribution of the 29 COSCATs with $\overline{FCO_2}$ comprised between -2 and $-1 \text{ mol C m}^{-2} \text{yr}^{-1}$, though more widespread around the globe, is also dominated by high Northern (Greenland, Western Europe, and Sea of Japan) and Southern latitudes (Southern America, Africa, Australia, and New Zealand). The 87 COSCATs with $\overline{FCO_2}$ comprised between -1 and $+1 \text{ mol C m}^{-2} \text{yr}^{-1}$ constitute the bulk of the continental shelf seas located between 30°S and 40°N and their cumulated surface area amounts to $14.7 \cdot 10^6 \text{ km}^2$. Antarctica and the Southern tip of Patagonia are the most notable shelves located outside of this latitude which range display moderate CO_2 exchange with the atmosphere. Except for the Gulf of Mexico and the Sea of Japan, marginal seas (Baltic Sea, Mediterranean Sea, Red Sea, and Sea Okhotsk) are weak sources of CO_2 (0 to $+1 \text{ mol C m}^{-2} \text{yr}^{-1}$) as are the majority of the Indian Ocean shelves. In contrast, Western Pacific shelves and most Northern Atlantic shelves are weak sinks of CO_2 (-1 to $0 \text{ mol C m}^{-2} \text{yr}^{-1}$). Only nine COSCATs display annual $\overline{FCO_2}$ higher than $+1 \text{ mol C m}^{-2} \text{yr}^{-1}$, and seven of them are located between 10°S and 20°N . The exceptions are the Northern tip of the Baltic Sea and the Sea of Okhotsk. The most intense source is located along the West African coast. Other significant sources of CO_2 are found in the Western Caribbean Sea, off the Brazilian coast, and along the Western Indian coasts.

The cumulated FCO_2 for the entire shelf seas amounts to a net sink of $185 \pm 46 \text{ Tg C yr}^{-1}$ ($0.19 \text{ Pg C yr}^{-1}$), and the aggregation of FCO_2 per MARCATs (Figure 2b and Table 2) reveals that the contribution of Arctic shelves to the global CO_2 sink is larger than that of any other oceanic basin. MARCATs 43 and 44 are two of the three the largest sinks in the world and, together with the Canadian Archipelagos and Northern Greenland

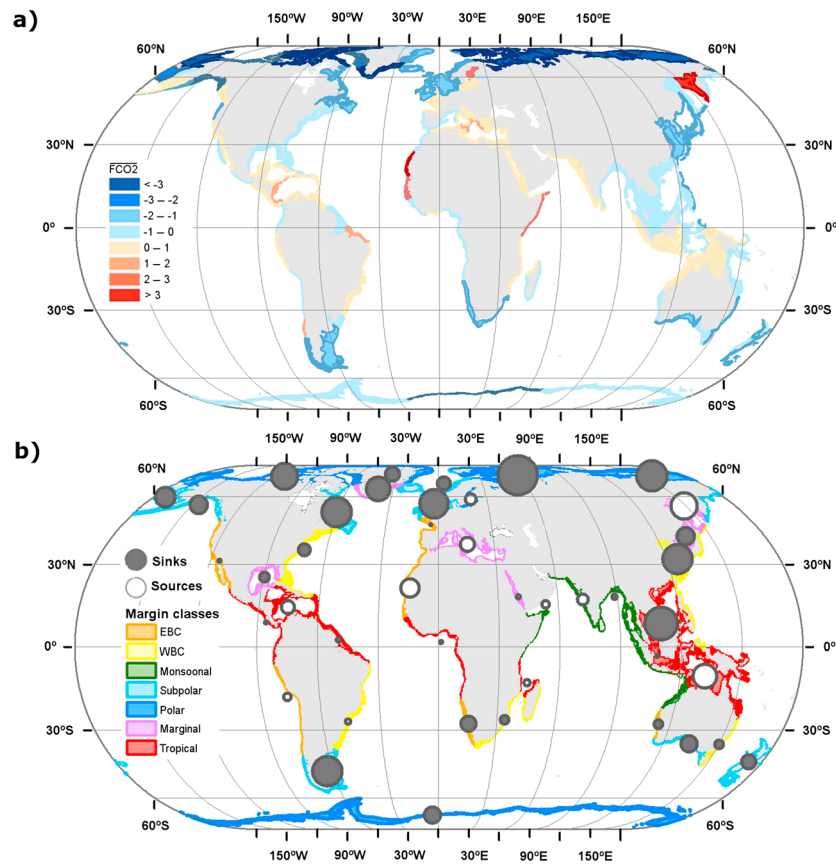


Figure 2. (a) $\overline{FCO_2}$ calculated for each COSCAT segment. Continental shelf classification as defined in *Laruelle et al.* [2013] and FCO_2 integrated per MARCATS, represented as pies. (b) The surface areas of the pies are proportional to the magnitude of the fluxes.

(MARCATS 13 and 14), Arctic shelves take up 71 Tg C yr^{-1} . North Atlantic shelves include the Sea of Labrador, South Greenland, and the Norwegian basin and the North Sea (MARCATS 11, 15, 16, and 17, respectively) and take up 34 Tg C yr^{-1} , while temperate and tropic Atlantic shelf seas are either small sinks (MARCATS 9, 10, 23, 24, and 15) or sources (MARCATS 6, 7, 8, 19, and 22), which never exceed 10 Tg C yr^{-1} , individually and combine for a quasi-neutral budget of $-0.1 \text{ Tg C yr}^{-1}$. At the Southern tip of the American continent, Patagonia (MARCATS 5) takes up 19 Tg C yr^{-1} because of its large surface area ($1.2 \cdot 10^6 \text{ km}^2$). Both the Baltic and Mediterranean seas that are connected to the Atlantic Ocean (MARCATS 18 and 20) are modest CO₂ sources (0.3 and 0.6 Tg C yr^{-1} , respectively). In the Indian Ocean, half of the shelves behave as sources of CO₂ (MARCATS 26, 27, 28, and 30). With the inclusion of the Red Sea, they all correspond to the monsoon-influenced margins [*Liu et al.*, 2010; *Laruelle et al.*, 2013]. The Bay of Bengal (MARCATS 31) and the tropical Eastern Indian shelves (MARCATS 32) are quasi-neutral CO₂ sinks ($<1 \text{ Tg C yr}^{-1}$). MARCATS 25 and 33 correspond to Eastern and Western boundary currents, respectively, which both behave as moderate CO₂ sinks ($<2 \text{ Tg C yr}^{-1}$). The Western Pacific display highly variable FCO_2 with the two largest sources worldwide in the North (Okhotsk Sea, MARCATS 41, 14 Tg C yr^{-1}) and the South (North Australian Shelves, MARCATS 37, 12 Tg C yr^{-1}) as well as two large CO₂ sinks ($>15 \text{ Tg C yr}^{-1}$; MARCATS 38, and 39). The other western pacific MARCATS (35, 36, 40, and 42) are also CO₂ sink of smaller magnitude ($<10 \text{ Tg C yr}^{-1}$), and the entire region combines for a sink of 36 Tg C yr^{-1} . On the other hand, the Eastern Pacific mainly consists in narrow shelves of limited surface areas characterized by quasi-neutral FCO_2 (MARCATS 2, 3, and 4), with the exception of the Bering Sea (MARCATS 1), which takes up 7 Tg C yr^{-1} . The Antarctic shelf seas (MARCATS 45) are an atmospheric sink of 5 Tg C yr^{-1} .

The latitudinal distribution of $\overline{FCO_2}$ (Figure 3a) shows that, north of 65°N , the values fall within the range -3.5 to $-2 \text{ mol C m}^{-2} \text{ yr}^{-1}$. Between 55°N and 10°S , the values oscillate with an increasing pattern from -1.5 to

Table 2. MARCATS, Their Cumulated Surface Areas and $\overline{FCO_2}$ ^a

Number	System Name	Class	Shelf Surface (10 ³ km ²)	Ice Cover (%)	$\overline{FCO_2}$ (Tg C yr ⁻¹)	Uncertainty ^b
1	North Eastern Pacific	Subpolar	461	0.0	-6.775	***
2	Californian Current	EBC	214	0.0	-0.135	** ***
3	Tropical Eastern Pacific	Tropical	198	0.0	0.192	* ** ***
4	Peruvian Upwelling Current	EBC	143	0.0	1.073	* **
5	Southern America	Subpolar	1230	0.0	-18.715	** ***
6	Brazilian Current	WBC	521	0.0	0.567	***
7	Tropical Western Atlantic	Tropical	517	0.0	0.394	*
8	Caribbean Sea	Tropical	344	0.0	3.460	* ** ***
9	Gulf of Mexico	Marginal Sea	544	0.0	-2.100	** ***
10	Florida Upwelling	WBC	858	0.6	-2.723	***
11	Sea of Labrador	Subpolar	395	16.0	-18.936	* ** ***
12	Hudson Bay	Margial Sea	1064	62.3	n.d.	-
13	Canadian Archipelagos	Polar	1177	78.7	-13.986	* **
14	Northern Groenland	Polar	614	73.6	-4.400	** ***
15	Southern Groenland	Polar	270	29.6	-11.972	** ***
16	Norwegian Basin	Polar	171	2.4	-3.342	***
17	North Eastern Atlantic	Subpolar	1112	0.7	-17.165	***
18	Baltic Sea	Marginal Sea	383	8.1	2.245	** ***
19	Iberian Upwelling	EBC	283	0.0	0.122	***
20	Mediterranean Sea	Marginal Sea	580	0.0	3.925	* ** ***
21	Black Sea	Marginal Sea	172	0.0	n.d.	-
22	Moroccan Upwelling	EBC	225	0.0	7.220	**
23	Tropical Eastern Atlantic	Tropical	284	0.0	-0.174	* **
24	Southern Western Africa	EBC	308	0.0	-5.103	**
25	Agulhas Current	WBC	254	0.0	-1.664	* ** ***
26	Tropical Western Indian	Tropical	72	0.0	0.815	*
27	Western Arabian Sea	Indian Margins	102	0.0	1.257	*
28	Rea Sea	Marginal Sea	190	0.0	0.330	* **
29	Persian Gulf	Marginal Sea	233	0.0	n.d.	-
30	Eastern Arabian Sea	Indian Margins	342	0.0	2.555	*
31	Bay of Bengal	Indian Margins	230	0.0	-0.530	*
32	Tropical Eastern Indian	Indian Margins	809	0.0	-0.170	* **
33	Leeuwin Current	EBC	118	0.0	-1.379	***
34	Southern Australia	Subpolar	452	0.0	-5.983	** ***
35	Eastern Australian Current	WBC	139	0.0	-1.695	***
36	New Zealand	Subpolar	283	0.0	-4.274	** ***
37	Northern Australia	Tropical	2463	0.0	12.120	** ***
38	South East Asia	Tropical	2318	0.0	-23.609	* **
39	China Sea and Kuroshio	WBC	1299	>0.1	-19.100	* ** ***
40	Sea of Japan	Marginal Sea	277	6.0	-6.113	** ***
41	Sea of Okhotsk	Marginal Sea	992	27.3	14.955	* **
42	North Western Pacific	Subpolar	1082	27.2	-8.419	* ** ***
43	Siberian Shelves	Polar	1918	84.1	-20.322	*
44	Barent and Kara Seas	Polar	1727	58.3	-32.225	* **
45	Antarctic Shelves	Polar	2952	76.0	-5.381	** ***

^an.d. corresponds to "no data."

^b*** (Three stars = good); ** (two stars = fair); * (one star = poor).

0.5 mol C m⁻² yr⁻¹. This is then followed by a decrease toward values < -1 mol C m⁻² yr⁻¹, south of 30°S. At around 60°S a peak of neutral $\overline{FCO_2}$ is observed and Antarctic shelves (-65°S to -80°S) are characterized by $\overline{FCO_2}$ around -0.8 mol C m⁻² yr⁻¹. The latitudinal distribution of continental shelf surface areas indicates the large contribution of Arctic (north of 65°N) and sub-Arctic shelves (55°N-60°N). Their cumulated surface area amounts to ~7 · 10⁶ km² (25%). The latitudinal distribution of $\overline{FCO_2}$ thus further evidences the disproportionate contribution of the Arctic shelves in the global C budget as a result of combined low $\overline{FCO_2}$ and high surface areas. The latitudinal distribution of $\overline{FCO_2}$ calculated individually for each COSCAT (Figure 4a) shows the extent of the dispersion around the average value (red curve). It reveals that heterogeneity is maximal at around 60°N and generally correlates with the shelf surface area. Aside from a handful of outliers, most $\overline{FCO_2}$ fall within the range ±2 mol C m⁻² yr⁻¹. Hence, variations within a climatic zone are lower than those between climatic zones. The

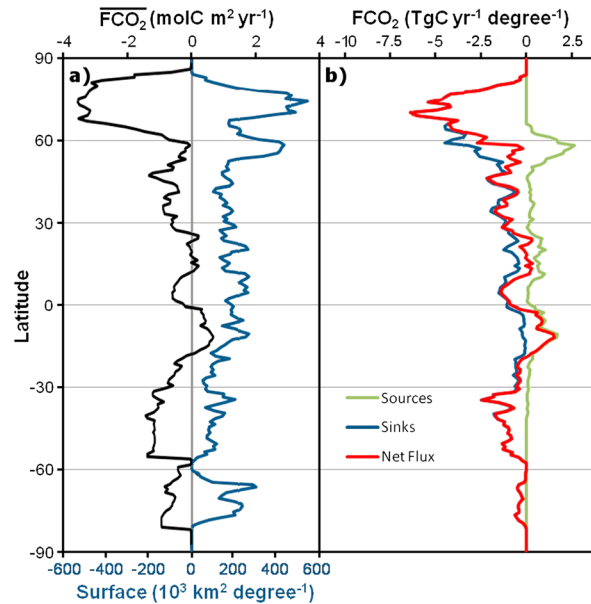


Figure 3. (a) Latitudinal profile of average $\overline{FCO_2}$ (black) and global continental shelf surface area (blue). (b) The integrated latitudinal FCO_2 profile displaying, per latitudinal band, the sources (green), sinks (blue), and net FCO_2 (red).

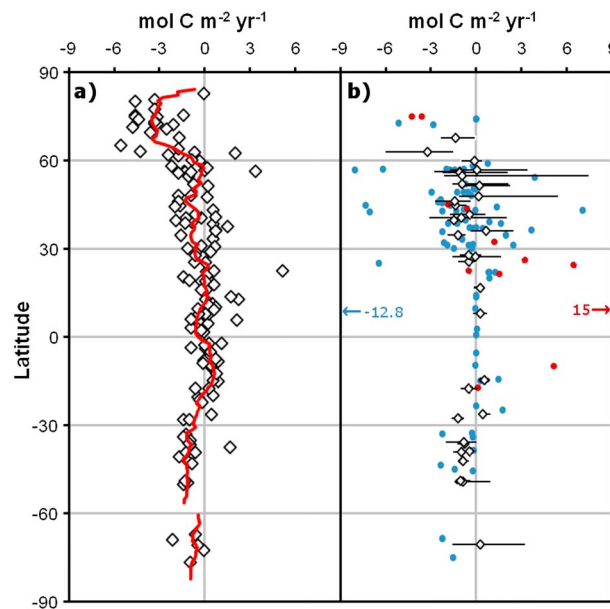


Figure 4. (a) Latitudinal distribution of yearly $\overline{FCO_2}$ calculated for each COSCAT (white diamonds) compared to the surface integrated latitudinal profile (red line). (b) COSCAT's $\overline{FCO_2}$ calculated using a 0.5° resolution grids as well as the range covered between the highest and lowest values within that COSCAT (represented as white diamonds and lateral bars, respectively). The blue dots correspond to local estimates of $\overline{FCO_2}$ extracted from the literature and used in previous shelf budgets [Borges *et al.*, 2005; Laruelle *et al.*, 2010; Chen *et al.*, 2013]. The red dots correspond to estimates reported as "coastal" in previous studies but located outside of the limits of the continental shelf.

variability within a COSCAT as evidenced in those for which $\overline{FCO_2}$ was calculated, from aggregation of 0.5° resolution values (Figure 4b) is much larger and of comparable magnitude to that of local $\overline{FCO_2}$ estimates reported in the literature.

3.2. Seasonal Dynamics of the Atlantic Shelf Seas

We define the geographic extent of the Atlantic Ocean from the Southern tip of Patagonia to the Northern shelves of the Labrador Sea, on the Western side, and from Cape Town to the Norwegian basin on the Eastern side (Figure 5). This delineation covers $7.9 \cdot 10^6 \text{ km}^2$, 62 COSCATs, and includes, at least partly, 14 MARCATs. We exclude internal marginal seas such as the Baltic and Mediterranean Seas but include the Caribbean Sea and the Gulf of Mexico, which are characterized by much larger exchanges with the Atlantic. Fifty-two COSCATs located within these limits possess sufficient data coverage to decipher the seasonal dynamics of $\overline{FCO_2}$ with a good confidence (three stars). Their cumulated surface area amounts to $5.6 \cdot 10^6 \text{ km}^2$. Figures 6a and 6e present the seasonal mean latitudinal profiles of $\overline{FCO_2}$. In this analysis, we use January, February, and March in the Northern Hemisphere and July, August, and September in the Southern Hemisphere to define winter and proceed in a similar fashion for other seasons. Winter and summer are presented together as the most contrasted seasons. Whereas spring and fall exhibit more consistent patterns in terms of climate and shelf productivity (Figures 6c and 6d), winter displays lower $\overline{FCO_2}$ than summer at all latitudes, except south of 45°S . Similarly, spring displays lower $\overline{FCO_2}$ than fall at almost all latitudes. For all seasons, $\overline{FCO_2}$ becomes more negative toward the poles and is maximal toward the equator in both hemispheres. Values are negative everywhere except in the 20°S – 20°N band, a range that expand slightly in summer in the Northern Hemisphere (up to about 45°N). The solubility of CO_2 in sea water expressed by Henry's constant (K'_0) is maximum at high latitudes and decreases by a factor 2 toward the equator

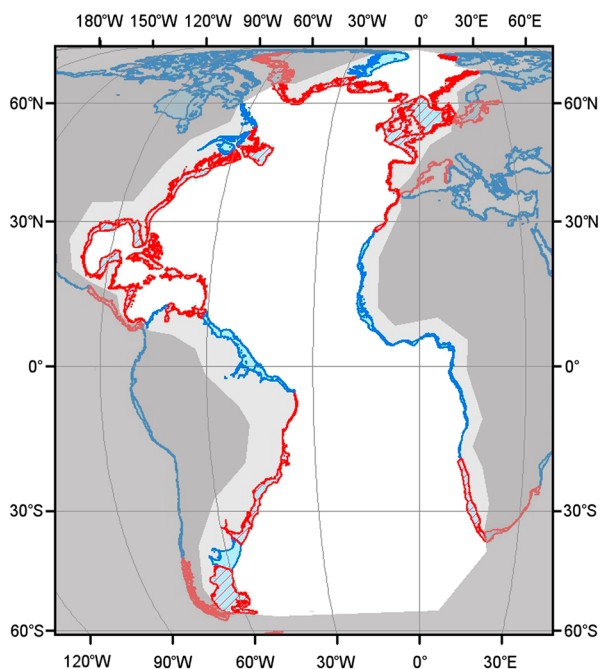


Figure 5. Geographic limits of the Atlantic Ocean used for this study. The dark blue line represents the limits of the COSCATs, and the superimposed dashed red line identifies the segments for which a seasonal $\overline{FCO_2}$ could be calculated.

(Figures 6b and 6f) independently of the season. In winter, K'_0 is generally higher than in summer, in particular, for northern temperate latitudes, while the difference in gas solubility between spring and fall is minimal. The latitudinal differences in water temperature (Figures 6c and 6g) between Polar Regions and the tropics is $>20^\circ\text{C}$ for all seasons. The difference between winter and summer temperature is significant at many latitudes and can exceed 10°C in the Northern Hemisphere. The temperature difference between spring and fall is generally small and never exceeds 4°C . Seasonal latitudinal profiles of Net Primary Production (NPP) on the shelf (Figures 6d and 6h) show rather heterogeneous distributions except in winter, where a clear latitudinal trend can be identified. Overall, the difference in NPP between summer and winter ($\Delta\text{NPP} < 1000 \text{ g C m}^{-2} \text{ yr}^{-1}$) is larger than that between spring and fall under temperate latitude

($\Delta\text{NPP} > 1000 \text{ g C m}^{-2} \text{ yr}^{-1}$). Summer is more productive than winter at high and temperate latitudes, and this trend is reversed between 35°N and 20°S . Except at low latitudes, where both seasons are about equally productive, the NPP in spring is consistently higher than that of fall by 500 to $1000 \text{ g C m}^{-2} \text{ yr}^{-1}$.

4. Discussion

4.1. Global Budget

With $-0.19 \text{ Pg C yr}^{-1}$, our new global estimate of the continental shelf CO_2 sink is slightly less negative than those reported in studies published over the last decade ($-0.37 \text{ Pg C yr}^{-1}$ in *Borges* [2005]; $-0.45 \text{ Pg C yr}^{-1}$ in *Borges et al.* [2005]; $-0.22 \text{ Pg C yr}^{-1}$ in *Cai et al.* [2006]; $-0.34 \text{ Pg C yr}^{-1}$ in *Chen and Borges* [2009]; $-0.21 \text{ Pg C yr}^{-1}$ in *Laruelle et al.* [2010]; $-0.36 \text{ Pg C yr}^{-1}$ in *Dai et al.* [2013]; and -0.40 in *Chen et al.* [2013]). These budgets were calculated using different estimates for the global surface area of continental shelf seas ranging from $24.7 \cdot 10^6 \text{ km}^2$ in *Laruelle et al.* [2010] to $30 \cdot 10^6 \text{ km}^2$ in *Chen and Borges* [2009]. None of these estimates accounts for the reduction of the surface of exchange with the atmosphere as a consequence of sea ice formation, which brings our effective surface area down to $22.3 \cdot 10^6 \text{ km}^2$. The resulting globally averaged flux density of $-0.7 \text{ mol C m}^{-2} \text{ yr}^{-1}$ is about 40% more negative than the averaged flux density of the open ocean evaluated to $-0.5 \text{ mol C m}^{-2} \text{ yr}^{-1}$ by *Wanninkhof et al.* [2013]. In that study, the coastal CO_2 sink was estimated at $-0.18 \text{ Pg C yr}^{-1}$ by extrapolating the flux density of the open ocean to the continental shelf. This value is remarkably close to our estimate of $-0.19 \text{ Pg C yr}^{-1}$ but is a consequence of the extrapolation to a larger surface area ignoring the ice cover. Our average flux density of $-0.7 \text{ mol C m}^{-2} \text{ yr}^{-1}$ is on par with those of *Cai et al.* [2006] and *Laruelle et al.* [2010] and sits at the least negative end of the -0.7 to $-1.4 \text{ mol C m}^{-2} \text{ yr}^{-1}$ range derived from previous studies. The factor 2 between these different estimates can likely be attributed to a bias toward industrialized regions in the older studies [*Borges et al.*, 2005; *Laruelle et al.*, 2010] to the inherent difficulty of extrapolating relatively scarce data to large areas that are very heterogeneous and to delineate consistent boundaries to carry a segmentation of the shelf [*Laruelle et al.*, 2010; *Cai*, 2011; *Chen et al.*, 2013; *Dai et al.*, 2013; *Laruelle et al.*, 2013]. In addition, the formulation and parametrization of the local flux estimations add an extra level of uncertainty. Numerous formulations of the gas transfer velocity k have been

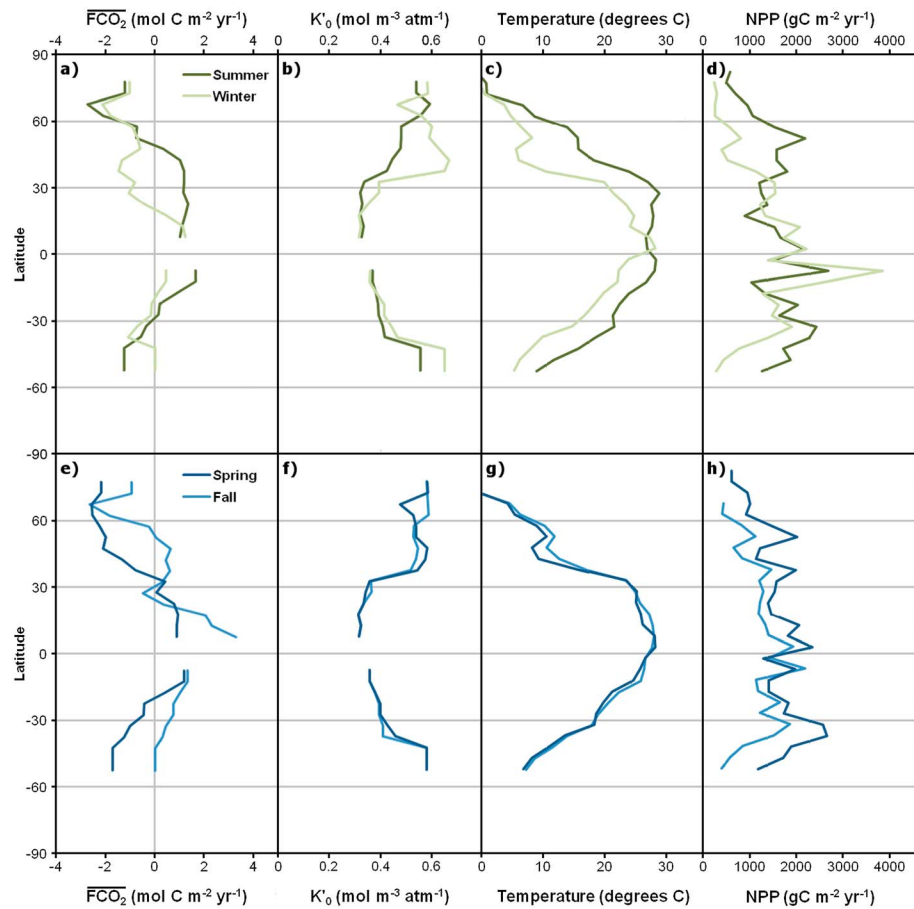


Figure 6. (a and e) Seasonal latitudinal profiles of $\overline{FCO_2}$, (b and f) Henry's constant K'_o , (c and g) water temperature, and (d and h) NPP for the continental shelves of the Atlantic Ocean. Figures 6a–6d correspond to summer and winter (in green), while Figures 6e–6h correspond to spring and fall (in blue). Temperature data are extracted from the World Ocean Atlas [Locarnini et al., 2010], and the NPP are derived from SeaWiFS data available for the 1997–2007 periods [Behrenfeld and Falkowski, 1997; Westberry et al., 2008].

proposed over the years [Wanninkhof, 1992; Wanninkhof and McGillis, 1999; Ho et al., 2006, 2011] and we selected the parameterization described in Ho et al. [2006] ($\Gamma = 0.26$ with k defined as $k = \Gamma C U^2 (\frac{Sc}{660})^{-1/2}$) and the one described in Wanninkhof [1992] ($\Gamma = 0.31$ k defined as $k = \Gamma C U^2 (\frac{Sc}{660})^{-1/2}$) to perform new FCO_2 calculations for each COSCAT (see supporting information). The two formulations yield global estimates for the coastal CO_2 uptake of $-0.18 \text{ Pg C yr}^{-1}$ and $-0.22 \text{ Pg C yr}^{-1}$ for Ho et al. [2006] and Wanninkhof [1992], respectively. Compared to our reference estimate of $-0.19 \text{ Pg C yr}^{-1}$ obtained using the formulation of Takahashi et al. [2009], this suggests that the uncertainty associated to the choice of different formulations of k may lead to variations in FCO_2 of $\sim 10\%$, as remarked by Ho et al. [2011]. This uncertainty remains low compared to the $\pm 0.05 \text{ Pg C yr}^{-1}$ confidence interval predicted by our calculations and largely resulting from the heterogeneity of the data distribution. Nonetheless, a relative uncertainty of 27% is a significant improvement over the estimates provided by previous studies, of the order of 50–100% [Laruelle et al., 2010; Cai, 2011; Regnier et al., 2013; Bauer et al., 2013]. Our approach, which provides regionalized FCO_2 calculated with globally consistent databases and mathematical formulations maintains consistency, optimizes spatiotemporal coverage, and gives our estimates relative uncertainties that reflect the method of integration. Note that the total number of COSCATs for which a temporal and spatially discrete FCO_2 could be calculated amounts to 52, which represents 36% of the surface area of continental shelf seas for which the uncertainty on the FCO_2 estimate can be considered good (three stars) or fair (two stars).

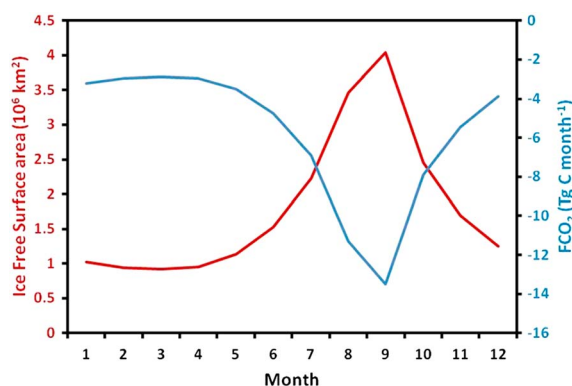


Figure 7. Seasonal evolutions of the cumulated ice-free surface area (in red) and the cumulated FCO_2 (in blue) of the Arctic shelves (MARCATS 13, 14, 43, and 44).

The very significant contribution of Arctic shelves to the global coastal carbon budget has already been pointed out in previous studies [Laruelle *et al.*, 2010; Cai, 2011] and can be explained by constantly cold water and Revelle factors as low as 3.5 to 6.5 in the Canadian Basin [Bates *et al.*, 2006]. Despite potential importance, the Arctic sink is still known with low confidence (*) because data density is limited in many parts of this ocean basin (only the Bering Sea and some sections of the Canadian Archipelagos are well covered). Our estimate of -71 Tg C yr^{-1} suggests that continental shelf waters contribute for a

significant fraction of the entire Arctic Ocean sink evaluated between -66 and $-199 \text{ Tg C yr}^{-1}$ in the literature [Bates and Mathis, 2009]. The role of sea ice cover as a main driver controlling the seasonal dynamics of FCO_2 in Arctic regions is evidenced by Figure 77. The cumulated surface area of the Arctic shelves is $5.4 \cdot 10^6 \text{ km}^2$, over which the sea ice cover oscillates between 83% in March and 26% in September. It is clear that the maximum CO_2 exchange takes place when the ice cover is the lowest. In light of the current trend of polar ice sheet to shrink as a consequence of global warming, it has been hypothesized that the Arctic Ocean could evolve toward a larger CO_2 sink [Bates *et al.*, 2006] and Arctic continental shelves could be significant contributors to this enhanced sink. Ignoring the ice cover entirely in our calculations would increase the sink in Arctic shelves threefold and lead to a global CO_2 uptake of $-0.34 \text{ Pg C yr}^{-1}$, comparable with the recent estimates of -0.36 and $-0.4 \text{ Pg C yr}^{-1}$ proposed by Dai *et al.* [2013] and Chen *et al.* [2013], respectively, which do not consider ice cover in their calculations. CO_2 exchange through the ice sheet have been reported [Bates and Mathis, 2009] and could justify ignoring ice cover, but this process may be restricted to thin ice layers and its overall importance remains difficult to quantify. Additionally, our estimation does not account either for near-shore CO_2 evasion of supersaturated waters brought by large Siberian Rivers [Parmentier *et al.*, 2013].

Temperate regions most commonly are moderate sinks of CO_2 ($0 \text{ mol C m}^{-2} \text{ yr}^{-1} < \overline{FCO_2} < 1 \text{ mol C m}^{-2} \text{ yr}^{-1}$), but variability is large within this latitudinal band. This can partly be explained by the wide range of climatic and physical conditions encountered between 30° and 60° in both hemispheres [Liu *et al.*, 2010]. The variability can be significant from one COSCAT to the other, as well as within individual COSCATs, as evidenced by Figure 4b. The variability in $\overline{FCO_2}$ within temperate COSCATs may be as high as $10 \text{ mol C m}^{-2} \text{ yr}^{-1}$ and generally falls in the $2\text{--}5 \text{ mol C m}^{-2} \text{ yr}^{-1}$ range, which is comparable to the variability in $\overline{FCO_2}$ reported within a given COSCAT in local studies (Table 3 and COSCATs 401, 403, 827, 1324, and 1410). Half of the COSCATs for which monthly integration at 0.5° resolution have been performed are located between 40°N and 55°N , and this latitudinal band is thus the most suitable for comparison with published local estimates. In COSCATs where at least two $\overline{FCO_2}$ estimates were found in the literature, the average $\overline{FCO_2}$ calculated by our most accurate integration method (i.e., Method 1, “three stars” confidence) usually falls within the range of reported values (Table 3). In COSCATs 807 and 828, for which the average $\overline{FCO_2}$ diverges from the literature, there is nonetheless an overlap between the range reported in the literature and the $\overline{FCO_2}$ range calculated here for all the cells within the COSCAT. In the Sea of Okhotsk, however, the FCO_2 produced by our calculations appears in total contradiction with the local literature. The Sea of Okhotsk has been identified as a sink of CO_2 for the atmosphere [Otsuki *et al.*, 2003], while the FCO_2 calculated for MARCATS 41 is a large source of CO_2 (15 Tg C yr^{-1}). The bulk of this flux comes from just one of the three COSCATs constituting MARCATS 41. COSCAT 1317 exhibits a particularly high $\overline{FCO_2}$ ($3.4 \text{ mol C m}^{-2} \text{ yr}^{-1}$) derived from a very limited number of measurements collected at the outer eastern limit of the sea and corresponding to a punctual upwelling deep water characterized by high pCO_2 [Zeng *et al.*, 2002]. In comparison, COSCAT 1319, which corresponds to the southern Sea of Okhotsk, displays negative $\overline{FCO_2}$ ($-0.89 \text{ mol C m}^{-2} \text{ yr}^{-1}$),

Table 3. Reported and Calculated $\overline{FCO_2}$ for 9 COSCATs for Which, Several Estimates Where Available in the Literature and the Highest Resolution Integration Method Was Used

COSCAT	Location	Reported $\overline{FCO_2}$ (mol C m ⁻² yr ⁻¹)	Calculated $\overline{FCO_2}$ [Minimum/Maximum] (mol C m ⁻² yr ⁻¹)
401	English Channel and Gulf of Biscay	-2.9 ^a , -2.3 ^b , -0.8 ^c , -0.15 ^d , 0 ^e , 0.3 ^f	0.19 [-1.06/5.31]
403	North Sea	-1.7 ^f , -0.7 ^g	-1.28 [-2.14/1.99]
404	Baltic Sea	-0.8 ^h , 0.9 ⁱ	0.02 [-1.63/3.31]
807	Californian Coast	0.05 ^j , 0.5 ^j	0.77 [-0.29/2.4]
808	Oregon Coast	-7.3 ^k , -0.27 ^l	-1.61 [-1.77/-0.71]
827	North East US Coast	-1.8 ^m , -1.2 ^m , -0.68 ⁿ , 0 ^o , 1.42 ^p	-0.56 [-1.67/0.55]
828	South East US Coast	-0.89 ^q , -0.48 ^r , -0.16 ^s	-0.10 [-1.5/1.57]
1324	North East China Sea	-2.4 ^t , -1.80 ^u , -0.87 ^v	-1.53 [-1.80/-0.76]
1410	East Australia	-2.3 ^w , -0.17 ^x	-1.02 [-1.93/-0.05]

^aFrankignoulle and Borges, 2001.

^bde la Paz et al., 2010.

^cBorges et al., 2006.

^dThomas et al., 2007.

^eBorges and Frankignoulle, 2003.

^fThomas et al., 2004.

^gSchiettecatte et al., 2007.

^hThomas and Schneider, 1999.

ⁱWesslander et al., 2010.

^jFriederich et al., 2002.

^kHales et al., 2005.

^lSabine et al., 2011.

^mDegrandpré et al., 2002.

ⁿBoehme et al., 1998.

^oSalisbury et al., 2009.

^pShadwick et al., 2011.

^qSignorini et al., 2013.

^rJiang et al., 2008.

^sSabine et al., 2012.

^tTsunogai et al., 1999.

^uTseng et al., 2014.

^vShim et al., 2007.

^wBorges et al., 2008.

^xMcNeil, 2010.

consistent with the flux reported by Otsuki et al. [2003]. The surface area of COSCAT 1319 being 4 times smaller than that of COSCAT 1317, its contribution to the FCO_2 of the entire MARCATS 41 remains limited, in spite of a better data coverage. This example illustrates the limitation of our approach and the uncertainty associated to FCO_{2S} calculated for largely undersampled regions ("one star" confidence).

In our budget, equatorial and subtropical regions exhibit close to equilibrium conditions with respect to the atmosphere. This is evidenced by the quasi-neutral $\overline{FCO_2}$ for most COSCATs and the small dispersion around the average value within a given COSCAT (Figure 4b). These regions have been identified as mild CO_2 sources in previous studies [Borges et al., 2005; Laruelle et al., 2010], partly because coastal upwellings and large river plumes both acting as significant sources of CO_2 toward the atmosphere were included in the budget. However, although outgassing may occur only a few kilometers away from the land, the bulk of it does not necessarily take place within the limits of the continental shelf. This is especially true for coastal upwellings which generally develop on very narrow shelves. Additionally, not all upwelling regions behave as CO_2 sources all year long, and the nutrients provided by deep waters may trigger phytoplanktonic blooms resulting in CO_2 uptake. The outliers identified in red on Figure 4b correspond to local estimates included in previous coastal CO_2 budgets which are in fact located outside of the limits of the continental shelf as defined here. These points are often characterized by large positive $\overline{FCO_2}$ values. Therefore, while we agree that upwelling regions may emit large amounts of CO_2 [Liu et al., 2010], a large fraction of which is emitted outside of the boundaries of the continental shelf. Overall, there is little doubt that, equatorial regions may locally emit significant amounts of CO_2 to the atmosphere. Our calculations suggest, however, that these emissions could contribute only marginally to the global CO_2 budget.

4.2. Seasonality

The analysis performed for Atlantic shelves (Figure 6) allows investigating the respective influences of water temperature and NPP on the seasonality of FCO_2 . While other processes such as vertical mixing or the production of calcium carbonate by coccolithophores and foraminifera also contribute to the dynamics of CO_2 and may locally be dominant, seasonal water temperature changes and phytoplankton production are generally the main factors controlling the seasonal variations of pCO_2 [Chen *et al.*, 2013; Sarmiento and Gruber, 2006]. The roles of water temperature and NPP as major drivers of the seasonal $\overline{FCO_2}$ dynamics have been evidenced in several coastal systems [Thomas *et al.*, 2004; Shadwick *et al.*, 2010; Rysgaard *et al.*, 2012]. An increase in water temperature induces a decrease in gas solubility and a higher water pCO_2 , which pushes $\overline{FCO_2}$ toward positive values. On the other hand, an increase in NPP through stimulation of the “biological pump” lowers marine pCO_2 . A fraction of the biologically fixed carbon may subsequently be exported to the open ocean or the sediment [Walsh, 1988; Wollast, 1998; Mackenzie *et al.*, 2012], thus providing negative $\overline{FCO_2}$ values. The data coverage around the equator is not sufficient to draw any conclusion concerning the seasonality. In contrast, for temperate and high latitudes, our results highlight that the magnitude of seasonal $\overline{FCO_2}$ changes is comparable to the latitudinal difference in annually integrated $\overline{FCO_2}$ between polar and tropical systems. In spring the most negative $\overline{FCO_2}$ are observed, which are directly followed by the most $\overline{FCO_2}$ positive values in summer. A gradual decrease in FCO_2 from the summer maximum is observed in fall and winter. This classical seasonal dynamics have already been observed in many well-studied temperate shelves such as the North Sea [Frankignoulle and Borges, 2001; Thomas *et al.*, 2005] or the Eastern coast of the U.S. [Degrandpré *et al.*, 2002; Jiang *et al.*, 2008; Shadwick *et al.*, 2010]. Our analysis reveals that this pattern is also present at the global scale and can largely be explained by the interplay of seasonal temperature changes and NPP variations. The large difference between the $\overline{FCO_2}$ latitudinal profile in winter and summer strongly follows the water temperature difference between the two seasons, which translates into significant changes in gas solubility of CO_2 , especially for temperate latitudes. On Figure 6, the increase in water temperature between winter and summer can be correlated to a decrease in solubility and is associated to the highest $\overline{FCO_2}$ values. In contrast, the temperature difference between spring and fall is minimal, as is the change in solubility, and the comparatively lower spring $\overline{FCO_2}$ values are likely due to higher NPP. These observations suggest that the first-order seasonal dynamics of shelf CO_2 exchanges at the air-water interface can largely be explained by these two environmental forcings. Our synthesis also suggests that the solubility pump could be quantitatively more important than the biological pump in many regions around the globe as indicated by the seasonal changes in $\overline{FCO_2}$ observed for temperate latitudes, which appear to only be controlled by NPP variations when the changes in temperature and solubility are negligible. Such a strong dependency of CO_2 exchange to seasonal variations in temperature suggests large potential interannual variability, in particular, during years characterized by large-scale temperature anomalies such as El Niño or the North Atlantic Oscillation. Regional analysis of the effect of such events have already been performed [Thomas *et al.*, 2008; Fennel, 2010], but global extrapolations remain to be proposed.

Acknowledgments

This work relies on data extracted from the SOCAT v2.0 data product (<http://www.socat.info/>, Bakker *et al.* [2014]), the SOCAT/MARCATS segmentation [Laruelle *et al.*, 2013], the World Ocean Atlas [Antonov *et al.*, 2010; Locarnini *et al.*, 2010], the CCMP wind database [Atlas *et al.*, 2011], GLOBALVIEW CO₂ (<http://www.esrl.noaa.gov/gmd/ccgg/globalview/>), 25 km resolution monthly ice concentrations over the 1990–2011 provided by the NSIDC (National Snow and Ice Cover Data) [Cavalieri *et al.*, 1996] and NPP estimates derived from SeaWiFS from the Ocean Productivity website (<http://www.science.oregonstate.edu/ocean.productivity>). The authors also thank the SOCAT community for the early communication of their database and their technical support, Jean-Louis Tison for his advice regarding ice cover and Julie Rotschi for her contribution to the development of the methodology used in this study. The research leading to these results has received funding from the European Union's Seventh Framework Program (FP7/2007–2013) under grant agreement 283080, project GEOCARBON, and by the government of the Brussels-Capital Region (Brains Back to Brussels award to PR). Goulven G. Laruelle is ‘Chargé de recherches du F.R.S.-FNRS’ at the Université Libre de Bruxelles.

References

- Antonov, J. I., D. Seidov, T. P. Boyer, R. A. Locarnini, A. V. Mishonov, H. E. Garcia, O. K. Baranova, M. M. Zweng, and D. R. Johnson (2010), in *World Ocean Atlas 2009, Volume 2: Salinity*, NOAA Atlas NESDIS, vol. 69, edited by S. Levitus, U.S. Gov. Print. Off., Washington, D. C.
- Atlas, R., R. N. Hoffman, J. Ardizzone, S. M. Leidner, J. C. Jusem, D. K. Smith, and D. Gombos (2011), A cross-calibrated, multiplatform ocean surface wind velocity product for meteorological and oceanographic applications, *Bull. Am. Meteorol. Soc.*, *92*, 157–174, doi:10.1175/2010BAMS2946.1.
- Bakker, D. C. E., et al. (2014), An update to the Surface Ocean CO₂ Atlas (SOCAT version 2), *Earth Syst. Sci. Data*, *6*, 69–90, doi:10.5194/essd-6-69-2014.
- Bates, N. R., and J. T. Mathis (2009), The Arctic Ocean marine carbon cycle: Evaluation of air-sea CO₂ exchanges, ocean acidification impacts and potential feedbacks, *Biogeosciences*, *6*, 2433–2459, doi:10.5194/bg-6-2433-2009.
- Bates, N. R., S. B. Moran, D. A. Hansell, and J. T. Mathis (2006), An in-creasing CO₂ sink in the Arctic Ocean due to sea-ice loss, *Geophys. Res. Lett.*, *33*, L23609, doi:10.1029/2006GL027028.
- Bauer, J. E., W.-J. Cai, P. A. Raymond, T. S. Bianchi, C. S. Hopkinson, and P. A. G. Regnier (2013), The changing carbon cycle of the coastal ocean, *Nature*, *504*, 61–70, doi:10.1038/nature12857.
- Behrenfeld, M. J., and P. G. Falkowski (1997), Photosynthetic rates derived from satellite-based chlorophyll concentration, *Limnol. Oceanogr.*, *42*(1), 1–20.
- Boehme, S. E., C. L. Sabine, and C. E. Reimers (1998), CO₂ fluxes from a coastal transect: A time-series approach, *Mar. Chem.*, *63*, 49–67, doi:10.1016/S0304-4203(98)00050-4.
- Borges, A. V. (2005), Do we have enough pieces of the jigsaw to integrate CO₂ fluxes in the coastal ocean?, *Estuaries*, *28*(1), 3–27.
- Borges, A. V., and M. Frankignoulle (2003), Distribution of surface carbon dioxide and air-sea exchange in the English Channel and adjacent areas, *J. Geophys. Res.*, *108*(C8), 3140, doi:10.1029/2000JC000571.

- Borges, A. V., B. Delille, and M. Frankignoulle (2005), Budgeting sinks and sources of CO₂ in the coastal ocean: Diversity of ecosystems counts, *Geophys. Res. Lett.*, *32*, L14601, doi:10.1029/2005GL023053.
- Borges, A. V., L. S. Schiettecatte, G. Abril, B. Delille, and F. Gazeau (2006), Carbon dioxide in European coastal waters, *Estuarine Coastal Shelf Sci.*, *70*(3), 375–387, doi:10.1016/j.ecss.2006.05.046.
- Borges, A. V., B. Tilbrook, N. Metzl, A. Lenton, and B. Delille (2008), Inter-annual variability of the carbon dioxide oceanic sink south of Tasmania, *Biogeosciences*, *5*, 141–155.
- Cai, W.-J. (2011), Estuarine and coastal ocean carbon paradox: CO₂ sinks or sites of terrestrial carbon incineration?, *Ann. Rev. Mar. Sci.*, *3*, 123–145, doi:10.1146/annurev-marine-120709-142723.
- Cai, W.-J., Z. A. Wang, and Y. Wang (2003), The role of marsh-dominated heterotrophic continental margins in transport of CO₂ between the atmosphere, the land-sea interface and the ocean, *Geophys. Res. Lett.*, *30*(16), 1849, doi:10.1029/2003GL017633.
- Cai, W.-J., M. H. Dai, and Y. C. Wang (2006), Air sea exchange of carbon dioxide in ocean margins: A province based synthesis, *Geophys. Res. Lett.*, *33*, L12603, doi:10.1029/2006GL026219.
- Cavaliere, D. J., C. L. Parkinson, P. Gloersen, and H. Zwally (1996), Sea Ice Concentrations from Nimbus-7 SMMR and DMSP SSM/I-SSMIS Passive Microwave Data, years 1990–2011, NASA DAAC at the Natl. Snow and Ice Data Cent., Boulder, Colo. [Updated yearly.]
- Chen, C. T. A., and A. V. Borges (2009), Reconciling opposing views on carbon cycling in the coastal ocean: Continental shelves as sinks and near-shore ecosystems as sources of atmospheric CO₂, *Deep Sea Res., Part II*, *56*(8–10), 578–590, doi:10.1016/j.dsr2.2009.01.001.
- Chen, C. T. A., T. H. Huang, Y. C. Chen, Y. Bai, X. He, and Y. Kang (2013), Air-sea exchanges of CO₂ in the world's coastal seas, *Biogeosciences*, *10*, 6509–6544, doi:10.5194/bg-10-6509-2013.
- Dai, M., Z. Cao, X. Guo, W. Zhai, Z. Liu, Z. Yin, Y. Xu, J. Gan, J. Hu, and C. Du (2013), Why are some marginal seas sources of atmospheric CO₂?, *Geophys. Res. Lett.*, *40*, 2154–2158, doi:10.1002/grl.50390.
- de la Paz, M., X. A. Padín, A. F. Ríos, and F. F. Pérez (2010), Surface fCO₂ variability in the Loire plume and adjacent shelf waters: High spatio-temporal resolution study using ships of opportunity, *Mar. Chem.*, *118*, 108–118, doi:10.1016/j.jmarsys.2006.11.011.
- Degrandpré, M. D., G. J. Olbu, M. Beatty, and T. R. Hammar (2002), Air-sea CO₂ fluxes on the US Middle Atlantic Bight, *Deep Sea Res., Part II*, *49*, 4355–4367, doi:10.1016/S0967-0645(02)00122-4.
- Fennel, K. (2010), The role of continental shelves in nitrogen and carbon cycling: Northwestern North Atlantic case study, *Ocean Science*, *6*, 539–548, doi:10.5194/os-6-539-2010.
- Frankignoulle, M., and A. V. Borges (2001), European continental shelf as a significant sink for atmospheric carbon dioxide, *Global Biogeochem. Cycles*, *15*(3), 569–576, doi:10.1029/2000GB001307.
- Friederich, G. E., P. M. Walz, M. G. Burczynski, and F. P. Chavez (2002), Inorganic carbon in the central California upwelling system during the 1997–1999 El Niño-La Niña event, *Prog. Oceanogr.*, *54*(1–4), 185–203, doi:10.1016/S0079-6611(02)00049-6.
- GLOBALVIEW-CO₂ (2012), Cooperative atmospheric data integration project—Carbon dioxide, NOAA ESRL, Boulder, Colo. [Available at <http://www.esrl.noaa.gov/gmd/ccgg/globalview/>, last accessed December 15th 2013.]
- Hales, B., T. Takahashi, and L. Bandstra (2005), Atmospheric CO₂ uptake by a coastal upwelling system, *Global Biogeochem. Cycles*, *19*, GB1009, doi:10.1029/2004GB002295.
- Ho, D. T., C. S. Law, M. J. Smith, P. Schlosser, M. Harvey, and P. Hill (2006), Measurements of air-sea gas exchange at high wind speeds in the Southern Ocean: Implications for global parameterizations, *Geophys. Res. Lett.*, *33*, L16611, doi:10.1029/2006GL026817.
- Ho, D. T., R. Wanninkhof, P. Schlosser, D. S. Ullman, D. Hebert, and K. F. Sullivan (2011), Toward a universal relationship between wind speed and gas exchange: Gas transfer velocities measured with 3He/SF₆ during the Southern Ocean gas exchange experiment, *J. Geophys. Res.*, *116*, C00F04, doi:10.1029/2010JC006854.
- Jiang, L.-Q., W.-J. Cai, R. Wanninkhof, Y. Wang, and H. Lüger (2008), Air-sea CO₂ fluxes on the U.S. South Atlantic Bight: Spatial and seasonal variability, *J. Geophys. Res.*, *113*, C07019, doi:10.1029/2007JC004366.
- Kalnay, E., et al. (1996), The NCEP/NCAR 40-year reanalysis project, *Bull. Am. Meteorol. Soc.*, *77*, 437–470.
- Laruelle, G. G., H. H. Dürr, C. P. Slomp, and A. V. Borges (2010), Evaluation of sinks and sources of CO₂ in the global coastal ocean using a spatially-explicit typology of estuaries and continental shelves, *Geophys. Res. Lett.*, *37*, L15607, doi:10.1029/2010GL043691.
- Laruelle, G. G., H. H. Dürr, R. Lauerwald, J. Hartmann, C. P. Slomp, N. Goossens, and P. A. G. Regnier (2013), Global multi-scale segmentation of continental and coastal waters from the watersheds to the continental margins, *Hydrol. Earth Syst. Sci.*, *17*, 2029–2051, doi:10.5194/hess-17-2029-2013.
- Liss, P. S., and P. G. Slater (1974), Flux of gases across the air-sea interface, *Nature*, *247*, 181–184, doi:10.1038/247181a0.
- Liu, K.-K., L. Atkinson, R. Quinones, and L. Talaue-McManus (2010), *Carbon and Nutrient Fluxes in Continental Margins*, Global Change—The IGBP Series, vol. 3, edited by K.-K. Liu et al., Springer, Berlin, Heidelberg.
- Locarnini, R. A., A. V. Mishonov, J. I. Antonov, T. P. Boyer, H. E. Garcia, O. K. Baranova, M. M. Zweng, and D. R. Johnson (2010), *World Ocean Atlas 2009, Volume 1: Temperature*, NOAA Atlas NESDIS, vol. 69, edited by S. Levitus, U.S. Gov. Print. Off., Washington, D. C.
- Mackenzie, F. T., E. H. De Carlo, and A. Lerman (2012), Coupled C, N, P, and O biogeochemical cycling at the land-ocean interface, in *Treatise on Estuarine and Coastal Science*, edited by J. J. Middelburg and R. Laane, Elsevier.
- McNeil, B. I. (2010), Diagnosing coastal ocean CO₂ inter-annual variability from a 40 year hydrographic time series station off the east coast of Australia, *Global Biogeochem. Cycles*, *24*, GB4034, doi:10.1029/2010GB003870.
- Meybeck, M. (1982), Carbon, nitrogen and phosphorus transport by world rivers, *Am. J. Sci.*, *282*, 401–450.
- Meybeck, M., H. H. Dürr, and C. J. Vörösmarty (2006), Global coastal segmentation and its river catchment contributors: A new look at land-ocean linkage, *Global Biogeochem. Cycles*, *20*, GB1590, doi:10.1029/2005GB002540.
- Otsuki, A. S., S. Watanabe, and S. Tsunogai (2003), Absorption of atmospheric CO₂ and its transport to the intermediate layer in the Okhotsk Sea, *J. Oceanogr.*, *59*, 709–717.
- Parmentier, F.-J. W., T. R. Christensen, L. L. Sørensen, S. Rysgaard, A. D. McGuire, P. A. Miller, and D. A. Walker (2013), The impact of lower sea-ice extent on Arctic greenhouse-gas exchange, *Nature Climate Change*, *3*, 195–202, doi:10.1038/nclimate1784.
- Pfeil, B., et al. (2013), A uniform, quality controlled Surface Ocean CO₂ Atlas (SOCAT), *Earth Syst. Sci. Data*, *5*, 125–143, doi:10.5194/essd-5-125-2013.
- Regnier, P., et al. (2013), Anthropogenic perturbation of the carbon fluxes from land to ocean, *Nat. Geosci.*, *6*(8), 597–607, doi:10.1038/NGEO1830.
- Rysgaard, S., J. Mortensen, T. Juul-Pedersen, L. L. Sørensen, K. Lennert, D. Søgaard, K. E. Arendt, and M. K. Sejr (2012), High air-sea CO₂ uptake rates in nearshore and shelf areas of Southern Greenland: Temporal and spatial variability, *Mar. Chem.*, *128–129*, 26–33, doi:10.1016/j.marchem.2011.11.002.
- Sabine, C., S. Maenner, and A. Sutton (2011), High-resolution ocean and atmosphere pCO₂ time-series measurements from mooring La-Push_125W_48N, Carbon Dioxide Information Analysis Center, Oak Ridge Natl. Lab., U.S. Dep. of Energy, Oak Ridge, Tenn.
- Sabine, C., S. Maenner, and A. Sutton (2012), High-resolution ocean and atmosphere pCO₂ time-series measurements from mooring CoastalMS_88W_30N, Carbon Dioxide Information Analysis Center, Oak Ridge Natl. Lab., U.S. Dep. of Energy, Oak Ridge, Tenn.

- Salisbury, J., D. Vandemark, C. Hunt, J. Campbell, B. Jonsson, A. Mahadevan, W. McGillis, and H. Xue (2009), Episodic riverine influence on surface DIC in the coastal Gulf of Maine, *Estuarine Coastal Shelf Sci.*, *82*, 108–118, doi:10.1016/j.ecss.2008.12.021.
- Sarmiento, J. L., and N. Gruber (2006), in *Ocean Biogeochemical Dynamics*, edited by J. L. Sarmiento and N. Gruber, Univ. Press, Princeton.
- Schiettecatte, L. S., H. Thomas, Y. Bozec, and A. V. Borges (2007), High temporal coverage of carbon dioxide measurements in the Southern Bight of the North Sea, *Mar. Chem.*, *106*(1–2), 161–173, doi:10.1016/j.marchem.2007.01.001.
- Shadwick, E. H., H. Thomas, A. Comeau, S. E. Craig, C. W. Hunt, and J. E. Salisbury (2010), Air-sea CO₂ fluxes on the Scotian Shelf: Seasonal to multi-annual variability, *Biogeosciences*, *7*, 3851–3867, doi:10.5194/bg-7-3851-2010.
- Shadwick, E. H., H. Thomas, K. Azetsu-Scott, B. J. W. Greenan, E. Head, and E. Horne (2011), Seasonal variability of dissolved inorganic carbon and surface water pCO₂ in the Scotian Shelf region of the Northwestern Atlantic, *Mar. Chem.*, *124*(1–4), 23–37, doi:10.1016/j.marchem.2010.11.004.
- Shim, J. H., D. S. Kim, Y. C. Kang, J. H. Lee, S. T. Jang, and C. H. Kim (2007), Seasonal variations in pCO₂ and its controlling factors in surface seawater of the northern East China Sea, *Cont. Shelf Res.*, *27*(20), 2623–2636, doi:10.1016/j.csr.2007.07.005.
- Signorini, S. R., A. Mannino, R. G. Najjar Jr., M. A. M. Friedrichs, W.-J. Cai, J. Salisbury, Z. Aleck Wang, H. Thomas, and E. Shadwick (2013), Surface ocean pCO₂ seasonality and sea-air CO₂ flux estimates for the North American east coast, *J. Geophys. Res. Oceans*, *118*, 5439–5460, doi:10.1002/jgrc.20369.
- Takahashi, T., et al. (2009), Climatological mean and decadal change in surface ocean pCO₂, and net sea-air CO₂ flux over the global oceans, *Deep Sea Res., Part II*, *56*, 554–577, doi:10.1016/j.dsr2.2008.12.009.
- Takahashi, T., S. Sutherland, and A. Kozyr (2012), Global ocean surface water partial pressure of CO₂ database: Measurements performed during 1957–2011 (Version 2011). ORNL/CDIAC-160, NDP-088(V2011), Carbon Dioxide Information Analysis Center, Oak Ridge Natl. Lab., U.S. Dep. of Energy, Oak Ridge, Tenn.
- Thomas, H., and B. Schneider (1999), The seasonal cycle of carbon dioxide in Baltic Sea surface waters, *J. Mar. Syst.*, *22*(1), 53–67, doi:10.1016/S0924-7963(99)00030-5.
- Thomas, H., Y. Bozec, K. Elkalay, and H. J. W. De Baar (2004), Enhanced open ocean storage of CO₂ from shelf sea pumping, *Science*, *304*(5673), 1005–1008, doi:10.1126/science.1095491.
- Thomas, H., Y. Bozec, H. J. W. de Baar, K. Elkalay, M. Frankignoulle, L.-S. Schiettecatte, G. Kattner, and A. V. Borges (2005), The carbon budget of the North Sea, *Biogeosciences*, *2*, 87–96, doi:10.5194/bg-2-87-2005.
- Thomas, H., et al. (2007), Rapid decline of the CO₂ buffering capacity in the North Sea and implications for the North Atlantic Ocean, *Global Biogeochem. Cycles*, *21*, GB4001, doi:10.1029/2006GB002825.
- Thomas, H., A. E. Friederike Prowe, I. D. Lima, S. C. Doney, R. Wanninkhof, R. J. Greatbatch, U. Schuster, and A. Corbière (2008), Changes in the North Atlantic Oscillation influence CO₂ uptake in the North Atlantic over the past 2 decades, *Global Biogeochem. Cycles*, *22*, GB4027, doi:10.1029/2007GB003167.
- Tseng, C.-M., P.-Y. Shen, and K.-K. Liu (2014), Synthesis of observed air–sea CO₂ exchange fluxes in the river-dominated East China Sea and improved estimates of annual and seasonal net mean fluxes, *Biogeosciences*, *11*, 3855–3870, doi:10.5194/bg-11-3855-2014.
- Tsunogai, S., S. Watanabe, and T. Sato (1999), Is there a “continental shelf pump” for the absorption of atmospheric CO₂?, *Tellus*, *51*, 701, doi:10.1034/j.1600-0889.1999.t01-2-00010.x.
- Walsh, J. J. (1988), *On the Nature of Continental Shelves*, edited by J. J. Walsh, Academic Press, San Diego, New York, Berkeley, Boston, London, Sydney, Tokyo, Toronto.
- Wanninkhof, R. (1992), Relationship between wind speed and gas exchange over the ocean, *J. Geophys. Res.*, *97*(C5), 7373–7382.
- Wanninkhof, R., and W. R. McGillis (1999), A cubic relationship between air–sea CO₂ exchange and wind speed, *Geophys. Res. Lett.*, *26*(13), 1889–1892, doi:10.1029/1999GL900363.
- Wanninkhof, R., et al. (2013), Global ocean carbon uptake: Magnitude, variability and trends, *Biogeosciences*, *10*, 1983–2000, doi:10.5194/bg-10-1983-2013.
- Weiss, R. F. (1974), CO₂ in water and seawater: The solubility of a non-ideal gas, *Mar. Chem.*, *2*, 203–215.
- Wesslander, K., A. Omstedt, and B. Schneider (2010), Inter-annual and seasonal variations in the air–sea CO₂ balance in the central Baltic Sea and the Kattegat, *Cont. Shelf Res.*, *30*(14), 1511–1521.
- Westberry, T., M. J. Behrenfeld, D. A. Siegel, and E. Boss (2008), Carbon-based primary productivity modeling with vertically resolved photoacclimation, *Global Biogeochem. Cycles*, *22*, GB2024, doi:10.1029/2007GB003078.
- Wollast, R. (1998), Evaluation and comparison of the global carbon cycle in the coastal zone and in the open ocean, in *The Sea, Vol. 10, The Global Coastal Ocean: Ideas and Observations on Progress in the Study of the Seas*, edited by K. H. Brink and A. R. Robinson, pp. 213–252, John Wiley, Hoboken, N. J.
- Zeng, J. Y., Y. Nojiri, P. P. Murphy, C. S. Wong, and Y. Fujinuma (2002), A comparison of dpCO₂ distributions in the northern North Pacific using results from a commercial vessel in 1995–1999, *Deep Sea Res., Part II*, *49*, 5303–5315.